Femtosecond laser ablation properties of Er^{3+} ion doped zinc-sodium tellurite glass

Thomas Mann, Robert Mathieson, Matthew Murray, Billy Richards, and Gin Jose

Citation: Journal of Applied Physics **124**, 044903 (2018); doi: 10.1063/1.5040947
View online: https://doi.org/10.1063/1.5040947
View Table of Contents: http://aip.scitation.org/toc/jap/124/4
Published by the American Institute of Physics

Femtosecond laser ablation properties of Er^{3+} ion doped zinc-sodium tellurite glass

Thomas Mann, Robert Mathieson, Matthew Murray, Billy Richards, and Gin Jose[a)]
School of Chemical and Process Engineering, University of Leeds, Leeds LS2 9JT, United Kingdom

(Received 22 May 2018; accepted 26 June 2018; published online 24 July 2018)

We report the femtosecond laser (100 fs, 800 nm) ablation properties of Er^{3+} ion doped zinc-sodium tellurite glass. Ablation thresholds in dependence of the beam radius (13.9 and 32.0 μm), pulse number, and Er^{3+} ion dopant concentration have been determined. The ablation rate and crater profile depended on the applied fluence. https://doi.org/10.1063/1.5040947

I. INTRODUCTION

For the continued development and miniaturisation of integrated optics, transitioning from long optical fibres to planar waveguides is a necessary step.[1] Out of the various optical materials investigated, tellurite-based glasses have proven to be particularly promising due to their high refractive index, low phonon energy, high rare earth solubility, and large emission bandwidth.[2,3] Rare-earth ions are often doped into the host glass to provide the unique spectroscopic properties required for photonic applications. For example, the superbroadband luminescence obtained in tellurite glasses is utilised by optical amplifiers and tunable lasers.[4,5] The fabrication of erbium doped waveguide amplifiers (EDWAs) is a particularly active area of research. This is due to the transition of erbium in its preferred trivalent bonding state from the ground state to the metastable first excited state ($^4I_{15/2} \rightarrow {}^4I_{13/2}$) occurring at 1.54 μm, which is a standard wavelength for telecommunications as it coincides with the low loss C-band window of silica.[6]

A variety of glass optical waveguide fabrication techniques have been explored and can be classified into two primary categories: index modification and thin film deposition.[1] Ultrafast lasers are used in several of these fabrication techniques. Laser inscription forms waveguides in a bulk or thin film glass by modifying the local refractive index with femtosecond laser irradiation.[7–11] The type of modification depends on both the laser and glass parameters and can be classified as either a smooth refractive index change, a birefringent refractive index modification, or voids due to microexplosions.[2] The ultrafast laser plasma doping (ULPD) technique has been used to incorporate a record high lifetime-density product of Er^{3+} ions as thin films into silica glass substrates without clustering, thus overcoming a key limitation of the other EDWA fabrication techniques.[12] This technique has also been proven for silica-on-silicon (SOS) substrates, which is particularly promising as it enables the use of technology developed for microelectronics.[13] In brief, ULPD forms thin films onto a substrate by ablating an Er^{3+} ion doped zinc-sodium tellurite (TZN) glass with femtosecond laser irradiation. The plume resulting from the ablated volume reacts with a substrate forming a superficial rare earth doped tellurite modified silica layer.[12] The laser fluence in relation to the target properties is a critical parameter as it must be above the ablation threshold, but not too high so that the plume consists of ions and nano-particles with the absence of micro-particles.[14,15] For controlled material processing, a detailed characterisation of the femtosecond laser-matter interaction is therefore of key importance. A characterisation of the ablation threshold and rate for Er^{3+} ion doped TZN glass is lacking in the literature and is the focus of this research. A basic optical and physical characterisation of the Er^{3+} ion doped TZN glass is presented first. Following this, we investigate the laser ablated crater morphology, ablation threshold, and ablation rate of the Er^{3+} ion doped TZN glass.

II. EXPERIMENTAL DETAILS

A. Sample preparation

Glasses with compositions of (80-x)TeO_2–10ZnO-10Na_2O-xEr_2O_3 ($x = 0.00$, 0.25, 0.50 0.75, 1.00, 1.25, 1.50) mol. %, denoted TZN for $x = 0$ and xErTZN otherwise were prepared using analytical grade chemicals (TeO_2, ZnO, Na_2O and Er_2O_3) of purity > 99.99% and synthesised using a conventional melt-quenching procedure. After the chemicals were weighed out in their molar masses, they were ground into a fine powder using a marble pestle and mortar. A gold crucible containing the glass constituents was placed in a furnace at 875 °C for 3 hours with a low oxygen flow rate (1–2 l/min) to drag vapour from within the chamber and keep the OH^- content of the glass low. The melt was then cast into a preheated brass mould, transferred into an annealing furnace, and kept at 295 °C for 4 hours to remove residual thermal and mechanical strains. The samples were then cooled down to room temperature by 0.5 °C/min. Finally, the samples are cut and polished until they reached optical quality for characterisation with dimensions of ~30 × 30 × 3 mm^3.

a)Electronic mail: G.Jose@leeds.ac.uk.

B. Characterisation

The amorphous nature of the glasses was examined by a X-ray diffractometer (D8, Bruker) using Cu-Kα radiation ($\lambda = 1.54$ Å) 40 kV and 40 mA, with the scanning angle 2θ range between 10° and 100°. The density was measured using a helium pycnometer (Pycnomatic ATC, Thermofisher Scientific). The refractive index was obtained from the critical angle using a prism coupler (2010/M, Metricon) fitted with a 633 nm laser. The absorption spectra from 380–1800 nm were measured using a computer aided two-beam spectrophotometer at a resolution of 0.25 nm (LAMBDA 950 UV/Vis/NIR, PerkinElmer). All measurements were performed at room temperature (~20 °C).

C. Ablation experiments

Laser ablation was performed in ambient conditions using a Ti-sapphire laser (Libra series, Coherent) with a central wavelength of 800 nm, pulse duration of 100 fs, and maximum repetition rate of 1 kHz. The laser energy was determined with a pyroelectric detector and energy meter (PE50-DIF-C and Starlite Energy Meter, Ophir) and controlled with a half-wave plate and beam splitting polariser. The desired number of pulses was applied using an optical shutter (SH05, ThorLabs) with the laser operating at a reduced frequency of 20 Hz. Prior to irradiation, the samples were cleaned in an ultrasonic bath with acetone and isopropanol. Sample positioning was performed on an XYZ motorised translation stage (A3200 Npaq controller and ABL1000 Air-Bearing Direct-Drive Linear Stages, Aerotech). Testing sites were separated by 0.3 mm to avoid overlap and ablation debris from neighbouring sites from interfering with measurements. The linearly polarised output beam of 6 mm was diaphragmed through a 5.5 mm aperture to avoid edge defects and then focussed at normal incidence onto the sample surface using a f = 100 mm achromatic doublet lens. Different spot sizes at the sample surface were achieved by positioning the sample before the focal plane. A long focal length lens was chosen for an easier characterisation of laser produced craters and a less critical sample positioning.

The pulse energies were measured from the average of 50 pulses prior to ablation and ranged from 11.4 to 137.8 μJ. According to the manufacturer, the pre-pulse and post-pulse contrast ratio of the laser was >1000:1 and >100:0, respectively. Even at the maximum applied energies, the pre- and post-pulse fluence at the sample surface was well below the ablation threshold and so had no effect on the measurements.

Beam spot sizes and threshold fluences were evaluated via the D2-lnF method,[16] using data measured ex-situ by differential interference contrast (DIC) microscopy (Axio Imager A1m, Zeiss). More detailed characterisation of the morphological changes of the laser irradiated areas was undertaken via scanning electron microscopy (SEM) (Hitachi TM3030 operating at 15 kV) and atomic force microscopy (AFM) operating in tapping mode (D3100 Atomic force microscope, Veeco Digital Instruments, with a nanoscope IVa controller and 14 nm nominal tip diameter). AFM data were analysed with the open source software Gwyddion.[17,18]

III. RESULTS AND DISCUSSION

A. Characterisation

The X-ray diffraction patterns of the glass samples did not show any sharp peaks but a broad halo in the range $20° < 2\theta < 40°$, confirming the amorphous nature of the samples. The introduction of 1.5 mol. % Er_2O_3 into the host TZN glass increased the density of the glass from 5.18 to 5.27 g/cm^3. The increase in density is a result of the replacement of TeO_2 by Er_2O_3, which has a higher molecular weight. Furthermore, the linear increase in density with Er^{3+} ion concentration indicates that the glass network resists the formation of non-bridging oxygen at the low doping concentrations of Er_2O_3 used. The refractive index of TZN was 2.048.

The increase in the Er^{3+} ion content caused a change in the colour of the glass samples from clear to deep pink. The colour variation is a consequence of the Er^{3+} ion having electronic excited states in the visible region. The optical absorption coefficients of the glasses as a function of the photon frequency ν were calculated by

$$\alpha(\nu) = \frac{A}{L}, \tag{1}$$

where L is the thickness of the sample and A is the absorbance measured using the spectrometer. The absorption spectra of TZN and 0.75ErTZN in the range of 380–1800 nm are shown in Fig. 1. TZN exhibits featureless absorption with an absorption baseline of approximately 0.11 cm^{-1} after the UV absorption edge at 387 nm (3.2 eV). The addition of Er^{3+} dopant ions gives rise to eleven prominent transitions from the ground state ($^4I_{15/2}$) to the different excited states, $^4I_{13/2}$, $^4I_{11/2}$, $^4I_{9/2}$, $^4F_{9/2}$, $^4S_{3/2}$, $^2H_{11/2}$, $^4F_{7/2}$, $^4F_{5/2}$, $^4F_{3/2}$, $^2H_{9/2}$, $^4G_{11/2}$ centred at the wavelengths 1531 (with a smaller peak at 1497), 976, 800, 653, 545, 522, 489, 452, 444, 407, and 380 nm. The energy levels of the Er^{3+} ion in the host are split due to the Stark effect, resulting in broadened transitions.[6] The other doping concentrations showed similar spectra, with the height of the peaks increasing with the concentration of Er^{3+} ions in the glass.

The optical transition and electronic band structure are examined by the absorption edge in the UV region. For

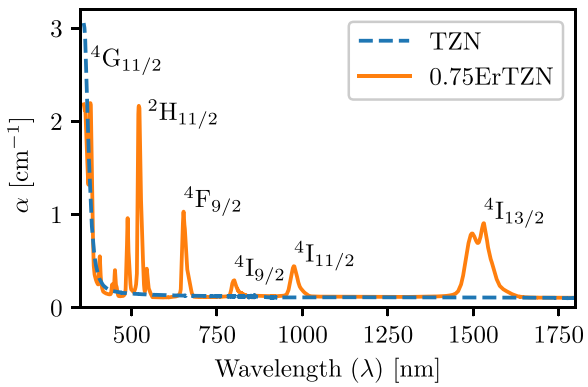

FIG. 1. Optical absorption spectra for TZN and 0.75ErTZN glasses. Text shows the Er^{3+} ion transitions from the ground state ($^4I_{15/2}$) giving rise to the peaks (only the prominent transitions are displayed for clarity, refer to the main text for all transitions).

direct and indirect transitions, electromagnetic waves excite the electrons in the valence band across the fundamental gap to the conduction band. According to Davis and Mott[19] the absorption coefficient, $\alpha(\nu)$, of amorphous materials can be expressed as a function of photon energy, $h\nu$, for the direct and indirect allowed transition by

$$\alpha(\nu) = B\frac{(h\nu - E_g)^n}{h\nu}, \tag{2}$$

where B is a constant, E_g is the band gap (direct or indirect), and n is the index number; $n = 1/2$ for direct allowed transitions and $n = 2$ for indirect allowed transitions. Both band gaps are interband transitions, but the latter involves a phonon interaction. The optical band gap values were obtained from the linear part of the curves and extrapolating to $(\alpha h\nu)^2 = 0$ and $(\alpha h\nu)^{1/2} = 0$ for direct and indirect transitions, respectively. Figures 2(a) and 2(b) show the Tauc plots and fitting procedure for TZN, giving a direct band gap value of 3.276 ± 0.023 eV and an indirect band gap value of 3.063 ± 0.012 eV.

Amorphous materials do not have a long range order and so the valence and conduction bands do not have a sharp cut off but rather tails of localised states. As a result, the absorption coefficient, $\alpha(\nu)$, near the optical band edge exhibits an exponential behaviour on the photon energy, $h\nu$, due to localised states extending into the band gap. The dependence is known as the Urbach empirical rule, which is given by[20]

$$\alpha(\nu) = \alpha_0 \exp(h\nu/\Delta E), \tag{3}$$

where α_0 is a constant and ΔE is the Urbach energy. The exponential behaviour is a result of the valence and conduction band tails extending into the band gap. The values of Urbach energy were calculated by taking the reciprocals of slopes of the linear portion of the high photon energy regions, as shown in Fig. 2(c). The Urbach energy was 0.1252 ± 0.0003 eV. The effect on the band gap and Urbach energy values due to the addition of Er^{3+} ions (if any) was within the error of measurement as the Er^{3+} ion transition $^4I_{15/2} \rightarrow {}^4G_{11/2}$ reduced the accuracy of the fitting procedure.

B. Ultrafast laser ablation

1. Crater morphology

Figure 3(a) presents AFM images and their respective cross-sectional profiles of craters ablated with a single laser pulse at energies 36.4, 56.8, and 88.4 μJ and a spot size of 32.0 μm. The single pulse craters had a shallow profile with an aspect ratio (depth divided by diameter) of ~0.02 and 0.01 for w_0 = 13.9 and 32.0 μm, respectively. At low energies, where the fluence was ≲2 J/cm^2, the craters take on a cylindrical profile. With increasing fluence, the craters transitioned to a Gaussian profile. A rim surrounding the craters, typically 20 to 50 nm in height, that extends upwards and increases in height with laser fluence is observed. Craters were also accompanied by radial splashes, seen clearly in the crater produced by an 88.4 μJ laser pulse in Fig. 3(a). These features are due to the formation of a thin molten zone below the ablated area and the pressure-driven flow generated by the plasma.[21] It could be the case that at low fluences the plasma pressure is not sufficient to eject the molten material from the crater and hence re-solidification of the melt results in a flat bottomed crater. This effect would be greater for TZN glasses as the volume of the molten material would be greater due to the low glass transition temperature when compared to other glasses [fused silica 1050 °C and borosilicate 593 °C (Ref. 22).]

The crater morphologies for several different fluences and irradiation with 10 or 32 pulses are shown in Fig. 4. Irradiation with 32 pulses close to the ablation threshold resulted in a ripple surface structure that is not seen with irradiation of 10 pulses [for example, compare Figs. 4(a) and 4(d)]. The ripples were most pronounced and homogeneous across the crater surface for fluences exceeding the multi-pulse ablation threshold by less than a factor of 5 (~0.85 J/cm^2). The ripple periodicity was ~1.4 μm, which is larger than the incident wavelength. Coarse ripples such as these are less commonly observed than fine ripples on transparent media.[23] Above this fluence, a peripheral nano-roughness is observed on the fringes of the craters [see Figs. 4(e) and 4(f)], where the Gaussian beam has a lower fluence. This is accompanied by a smooth melt feature central to the crater. At even higher fluences, a pillar-like macro feature that extends upward is observed, as shown in Fig. 4(f) (and confirmed via AFM). A similar crater profile was observed via SEM in fused silica after irradiation with 80, 220 fs duration

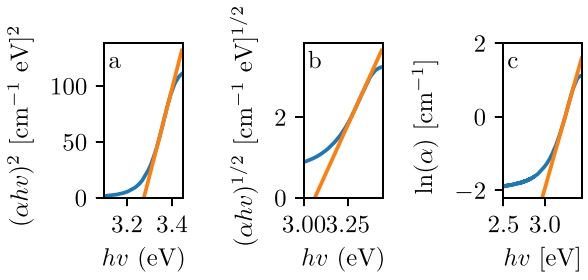

FIG. 2. Tauc plots to determine the direct (a), indirect band gaps (b), and Urbach energy (c) of TZN glass.

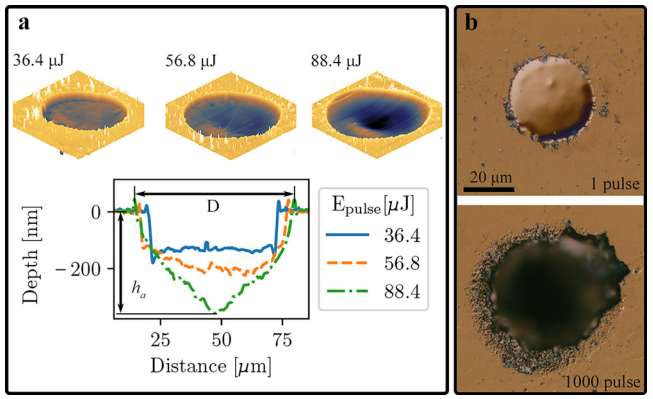

FIG. 3. (a) AFM profiles of craters produced on TZN by a single laser pulse at several energies and a spot size of 32.0 μm. On the cross sectional profiles, it is depicted how the crater diameter and height were determined, from which the 'effective optical penetration depth' and volume were calculated. (b) DIC micrographs of laser produced craters at a pulse energy of 45.8 μJ and spot size of 13.9 μm with different numbers of applied pulses.

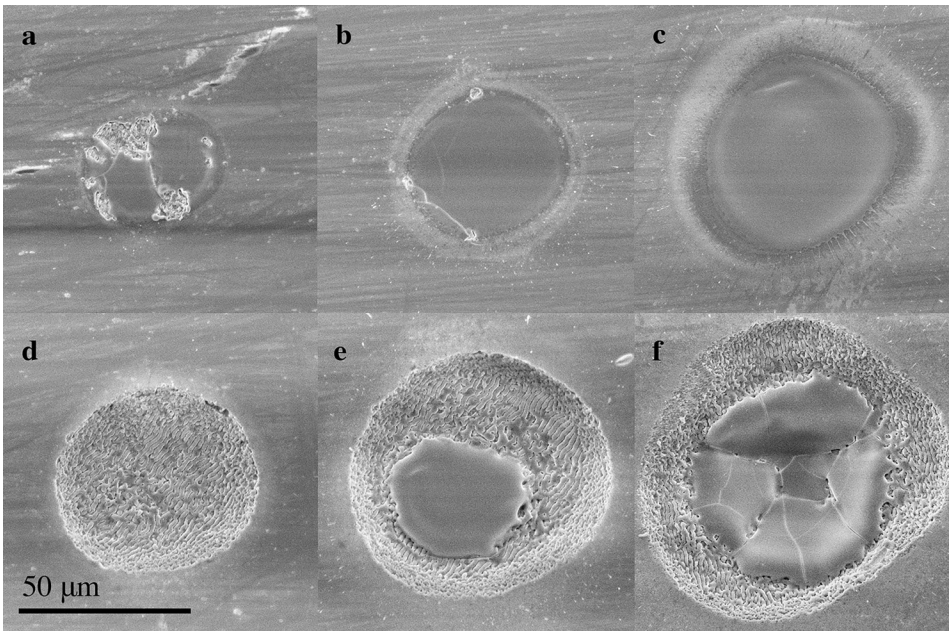

FIG. 4. SEM images (15 kV electron accelerating voltage) of multi-pulse ablation craters in TZN glass at a spot size of $w_0 = 32\,\mu$m. Top row 10 pulses per site (a)–(c) and bottom row 32 pulses per site (d)–(f). $E_{\text{pulse}} = 23.4\,\mu$J, $F_0^{\text{av}} = 0.73\,\text{J/cm}^2$ (a) and (d), $E_{\text{pulse}} = 36.4\,\mu$J, $F_0^{\text{av}} = 1.13\,\text{J/cm}^2$ (b) and (e) and $E_{\text{pulse}} = 137.8\,\mu$J, $F_0^{\text{av}} = 4.29\,\text{J/cm}^2$ (c) and (f).

pulses centred at a wavelength of 780 nm and fluence of 10.7 J/cm^2 by Lenzer *et al.*[22] This may be attributed to the inability of the molten material to escape the crater due to the increase in crater aspect ratio and solidifying as a 'splash' in the centre.[22]

2. Threshold fluence

The ablation threshold F_{th} (also known as damage threshold or threshold fluence) was determined from the linear relationship between the square of the crater diameter D and the logarithm of the average laser fluence F_0^{avg} (D2-LnF method)[16]

$$D^2(N) = 2w_0^2 \ln\left(\frac{F_0^{\text{avg}}}{F_{\text{th}}(N)}\right), \tag{4}$$

where w_0 is the $1/e^2$ laser beam radius for a Gaussian spatial beam profile and N is the number of pulses applied per sampling position. The average laser fluence of a Gaussian laser beam is related to the total pulse energy E_{pulse} through the relation $F_0^{\text{avg}} = E_{\text{pulse}}/(\pi w_0^2)$. Additionally, due to the linear dependence of the laser fluence on the pulse energy, w_0 may be calculated from the plot of the crater diameter squared against the logarithm of the pulse energy.

The ablation threshold is dependent on N due to the 'incubation effect', which occurs when the low fluence region of the laser beam, below the single shot ablation threshold, deposits energy into the material causing mechanical and/or chemical modifications.[24,25] As a result, defects are generated which lead to a lower ablation threshold. The generation of defects in dielectrics, such as F-centres, is experimentally found to saturate after a certain number of pulses causing the ablation threshold to remain constant with increasing pulse numbers. To quantify this, an accumulation model was proposed by Ashkenasi *et al.*[26]

$$F_{\text{th}}(N) = F_{\text{th}}(\infty) + [F_{\text{th}}(1) - F_{\text{th}}(\infty)]e^{-k(N-1)}, \tag{5}$$

where k is a parameter defining the rate at which the threshold fluence approaches the infinite pulse value. In our measurements, the linear relationship of Eq. (4) was observed up to ~10 times the ablation fluence. Above this fluence, D^2 showed an exponentially increasing dependence upon the logarithm of the fluence and this data was therefore not included in the analysis. The deviation at high fluences is due to a combination of excessive cracking in the glass, as shown in Fig. 3(b), due to mechanical modification by previous incubating pulses[27] and a deviation from the ideal Gaussian profile in the beam tails,[28] as shown in Fig. 4(f). Extrapolating the linear regression for each number of applied pulses using Eq. (4) yields the pulse dependent ablation threshold, as shown in Fig. 5(a). For both spot sizes the ablation threshold drops within the first 50 pulses to a limiting value that is approximately 40% of the single shot value and is well described by Eq. (5). This reduction is less than

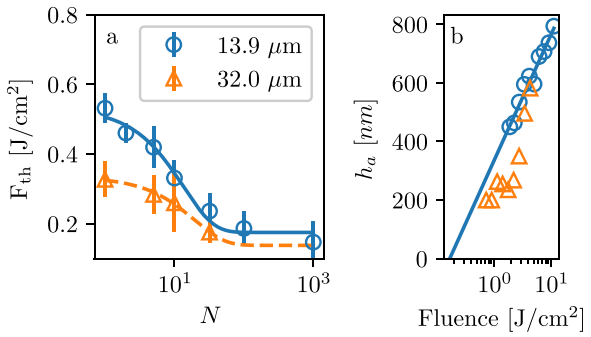

FIG. 5. (a) The multipulse threshold fluence dependence of TZN. Data are fitted with Eq. (5) with the parameters $F_{\text{th}}(1) = 0.51$, $F_{\text{th}}(\infty) = 0.18$, and $k = 0.074\,F_{\text{th}}\,(\infty)$ for $w_0 = 13.9\,\mu$m (solid line) and $F_{\text{th}}(1) = 0.32$, $F_{\text{th}}(\infty) = 0.14$, and $k = 0.051$ for $w_0 = 32.0\,\mu$m (dashed line). (b) The multipulse ablation threshold measurements of TZN glass as determined from the single pulse crater depth. The legend is the same as for (a). The plots presents the logarithmic dependence of the ablation rate h_a on the laser fluence F_0^{avg}. Extrapolation of Eq. (6) to zero gives a limiting multipulse threshold fluence of $F_{\text{th}}^{\infty} = 0.17 \pm 0.03\,\text{J/cm}^2$ and the gradient gives an effective optical penetration depth $\alpha_{\text{eff}}^{-1} = 187 \pm 15$.

for αSiO_2 where a 75% reduction in threshold fluence was observed from 3.7 J/cm^2 reduced to 0.9 J/cm^2 after 20 applied pulses[24] and borosilicate (in air) where a 76% reduction from 2.6 J/cm^2 to 1.74 J/cm^2 was measured.[29] The dependence of the ablation threshold on the spot size has been observed in dielectric thin films[30] and barium borosilicate glass[31] and is explained by realising that the ablation threshold is composed of two components; an intrinsic material ablation threshold and a defect ablation threshold component. The probability of the latter increases with beam size leading to an overall lower ablation threshold.

The limiting multipulse ablation threshold F_{th} (∞) may also be evaluated from the single pulse crater depth h_a so long as the fluences are well above the ablation threshold, so that steady state material removal occurs, by using the relation proposed by Ben-Yakar and Byer[29]

$$h_a = \alpha_{eff}^{-1} \ln\left(\frac{F_0^{avg}}{F_{th}(\infty)}\right), \tag{6}$$

where α_{eff}^{-1} is interpreted as the 'effective optical penetration depth' as expected from Beer-Lambert's law. This parameter primarily determines the volume in which the non-thermal femtosecond ablation processes take place. Extrapolation to zero for TZN glass at a spot size of 13.9 μm, as shown in Fig. 5(b), gives F_{th} (∞) = 0.17 ± 0.03 J/cm^2, which agrees well with the D2-LnF measurements. The effective optical penetration depth α_{eff}^{-1} = 187 ± 15 nm corresponds to an effective absorption coefficient of α_{eff} = 5.4 ± 0.4 × 10^4 cm^{-1}. The measured absorption coefficients are slightly higher than that for borosilicate glass exposed to 780 nm 200 fs laser pulses (α_{eff} = 4.2 × 10^4 cm^{-1}, α_{eff}^{-1} = 238 nm).[29]

3. Er^{3+} ion dopant

D2-LnF ablation threshold measurements of the Er^{3+} ion doped glass samples at a spot size of ~13.9 μm showed no trend with dopant concentration. The mean and standard deviation of the parameters to the fits of Eq. (5) for all glass samples were $F_{th}(1)$ = 0.51 ± 0.03 J/cm^2, $F_{th}(\infty)$ = 0.18 ± 0.01 J/cm^2, and k = 0.053 ± 0.009. This is to be expected at low doping concentrations for the following reasons. First, femtosecond laser ablation is a non-linear process owing to the highly intense laser field of the short pulse duration.[32] The band gap value is therefore one of the main parameters characterising this process and did not vary to any significant degree with Er^{3+} ion concentration. Second, at the highest 1.5 mol. % doping concentration the linear absorption at 800 nm was increased from 0.11 cm^{-1} for TZN to 0.85 cm^{-1}. The 'effective optical absorption coefficient' for the non-linear process had a value of 5.4 × 10^4 cm^{-1} for TZN, which is five orders of magnitude larger than the linear absorption coefficient, and it is therefore clear that the linear absorption is of no relevance. Finally, physical changes to the glass parameters such as density, refractive index, and melting point are small at low doping concentrations and are therefore not expected to modify the ablation threshold.

4. Ablation volume

As shown in Fig. 3(a), the profiles of the laser ablated craters depend on the applied fluence. In the Gaussian profile regime ($\gtrsim$ 2 J/cm^2), both D^2 and h_a each depend on the logarithm of the fluence and therefore, the volume is linear in the squared logarithm of the fluence. In the low fluence cylindrical regime, h_a was roughly constant at 210 nm ($\sim \alpha_{eff}^{-1}$) and the volume is therefore dependent on the logarithm of the fluence. The ablated volume is plotted as a function of the logarithm of the laser fluence in Fig. 6(a). A linear fit through the first three data points (low fluence cylindrical profile regime for w_0 = 32.0 μm) of single pulse craters and extrapolation to zero gives $F_{th}(1)$ = 0.38 and 0.621 J/cm^2 for w_0 = 32.0 and 13.8 μm, respectively. The values are overestimations of the values found via the D2-LnF method. This highlights why the ablation threshold determination via volume measurements can be less accurate as knowledge of the profile shape is required, which can change depending on the fluence regime. Coincidently, the ablation with single pulses at w_0 = 32.0 μm gave equivalent material removal rates with N = 5 at w_0 = 13.9 μm.

For micromachining and ULPD type applications, knowledge of the volume per unit input energy of the ablated material is of great importance. Figure 6(b) shows that below ~2 J/cm^2, or ~5 × F_{th} (1), the ablation rate is approximately flat at 6.8 ± 0.3 μm^3/μJ at a spot size of 32 μm. Between the

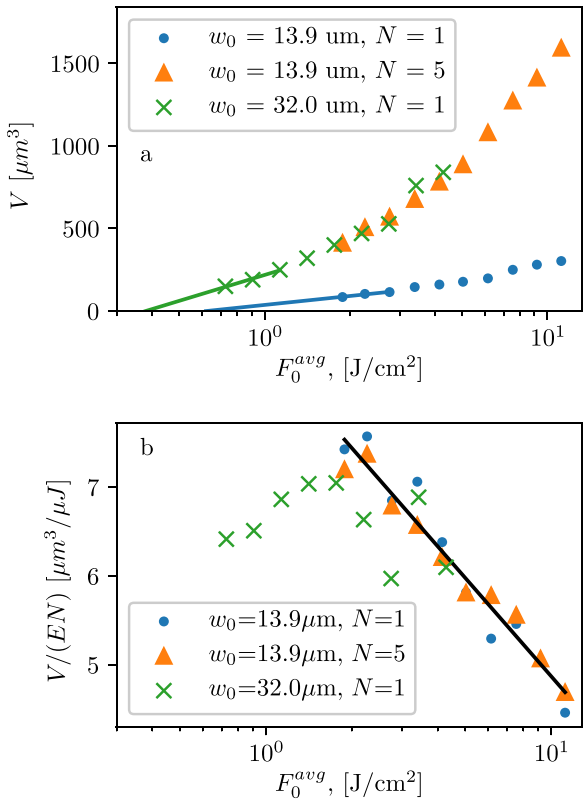

FIG. 6. (a) The volume of the ablated craters as a function of the logarithm of the laser fluence. A linear fit through the first three data points of single pulse craters and extrapolation to zero gives $F_{th}(1)$ = 0.38 and 0.621 J/cm^2 for w_0 = 32.0 and 13.8 μm, respectively. (b) Volume per pulse per unit of energy as a function of the logarithm of the laser fluence. A linear fit through the w_0 = 13.9 μm data (black line) has the equation –1.597x + 8.584.

range 2 and 11.5 J/cm^2, the ablation volume per unit input energy decreases with fluence from ~7.3 to 4.5 $\mu m^3/\mu J$. A reduction in ablation efficiency was observed by Perry *et al.*[33] for glass exposed to high fluences ($F_0 > 5–10 \times F_{th}$) due to a large portion of the incident energy being reflected back off the sample caused by an increase in the reflectivity of dielectrics at high laser fluences. The ablation rates are far higher than 1.5 $\mu m^3/\mu J$ observed for borosilicate glass irradiated with 200 fs laser pulses at 780 nm between $10 < F_0^{avg} < 40\,J/cm^2$.

IV. CONCLUSION

We have investigated the femtosecond laser ablation properties of Er^{3+} ion doped TZN glass. The direct band gap of TZN was 3.276 eV, which is just over twice the femtosecond laser photon energy (1.55 eV or 800 nm). The laser ablated crater profile depended on the applied fluence and pulse number. Below an average fluence of ~2 J/cm^2, the craters had a cylindrical profile and above this fluence, the craters had a Gaussian profile. The laser fluence and the number of the applied pulses determine whether nano- micro- or macro-structuring takes place. Ripples with a periodicity of ~1.4 μm were observed with multiple pulses close to the ablation threshold.

Measurements of the crater diameter at varying fluences yielded a single shot ablation threshold of 0.51 and 0.32 J/cm^2 at a spot size of 13.9 and 32.0 μm, respectively. The multipulse ablation threshold was found after approximately 50 applied pulses and was ~40% of the single pulse value. The ablation threshold was found to decrease with an increase in the the laser spot size at the surface due to an increase in the probability of the laser beam striking a defect in the glass. The ablation threshold did not change with the addition of up to 1.5 mol. % Er_2O_3 dopant concentration.

The amount of material removal per unit input energy is about 6.8 $\mu m^3/\mu J$ up to a fluence of 2 J/cm^2 and linearly decreasing from 7.3–4.5 $\mu m^3/\mu J$ in an intermediate fluence regime. The decrease in the ablated volume with increasing laser fluence indicates a reduced ablation efficiency at higher fluences, which may be attributed to an increased surface reflectivity.

ACKNOWLEDGMENTS

We would like to thank Dr. Paul Steenson and Dr. Christopher Russell, University of Leeds Electronic and Electrical Engineering department, for support in carrying out AFM measurements.

Thomas Mann would like to state that this work was supported by the Engineering and Physical Sciences Research Council (EPSRC) (DTP Award reference No. 1559338) and all authors acknowledge the support of EPSRC project Nos. EP/M015165/1 and EP/M022854/1.

[1]G. C. Righini and A. Chiappini, Opt. Eng. **53**, 071819 (2014).
[2]V. A. G. Rivera, D. Manzani, and V. A. G. Rivera, *Technological Advances in Tellurite Glasses* (Springer, 2017).
[3]S. Shen, A. Jha, X. Liu, M. Naftaly, K. Bindra, H. J. Bookey, and A. K. Kar, J. Am. Ceram. Soc. **85**, 1391 (2002).
[4]B. Zhou, L. Tao, Y. H. Tsang, W. Jin, and E. Y.-B. Pun, Opt. Express **20**, 3803 (2012).
[5]B. Zhou, L. Tao, W. Jin, Y. H. Tsang, and E. Y. B. Pun, IEEE Photonics Technol. Lett. **24**, 924 (2012).
[6]A. Polman, J. Appl. Phys. **82**, 1 (1997).
[7]L. Shah, A. Arai, S. Eaton, and P. Herman, Opt. Express **13**, 1999 (2005).
[8]S. Eaton, H. Zhang, P. Herman, F. Yoshino, L. Shah, J. Bovatsek, and A. Arai, Opt. Express **13**, 4708 (2005).
[9]A. Ferrer, A. R. de la Cruz, D. Puerto, W. Gawelda, J. A. Vallés, M. a. Rebolledo, V. Berdejo, J. Siegel, and J. Solis, J. Opt. Soc. Am. B **27**, 1688 (2010).
[10]V. Diez-Blanco, J. Siegel, A. Ferrer, A. Ruiz De La Cruz, and J. Solis, Appl. Phys. Lett. **91**, 051104 (2007).
[11]P. Nandi, G. Jose, C. Jayakrishnan, S. Debbarma, K. Chalapathi, K. Alti, A. K. Dharmadhikari, J. A. Dharmadhikari, and D. Mathur, Opt. Express **14**, 12145 (2006).
[12]J. Chandrappan, M. Murray, T. Kakkar, P. Petrik, E. Agocs, Z. Zolnai, D. P. Steenson, A. Jha, and G. Jose, Sci. Rep. **5**, 14037 (2015).
[13]S. A. Kamil, J. Chandrappan, M. Murray, P. Steenson, T. F. Krauss, and G. Jose, Opt. Lett. **41**, 4684 (2016).
[14]J. Perrière, C. Boulmer-Leborgne, R. Benzerga, and S. Tricot, J. Phys. D: Appl. Phys. **40**, 7069 (2007).
[15]P. Balling and J. Schou, Rep. Prog. Phys. **76**, 036502 (2013).
[16]J. M. Liu, Opt. Lett. **7**, 196 (1982).
[17]D. N. Y. P. Klapetek, see http://gwyddion.net/ for the software Gwyddion used for AFM image analysis, 2018.
[18]D. Nečas and P. Klapetek, Open Phys. **10**, 181 (2012).
[19]E. A. Davis and N. F. Mott, Philos. Mag. **22**, 903 (1970).
[20]F. Urbach, Phys. Rev. **92**, 1324 (1953).
[21]A. Ben-Yakar, A. Harkin, J. Ashmore, R. L. Byer, and H. A. Stone, J. Phys. D: Appl. Phys. **40**, 1447 (2007).
[22]M. Lenzner, F. Krausz, J. Krüger, and W. Kautek, Appl. Surf. Sci. **154**, 11 (2000).
[23]R. Buividas, M. Mikutis, and S. Juodkazis, Prog. Quantum Electron. **38**, 119 (2014).
[24]A. Rosenfeld, M. Lorenz, R. Stoian, and D. Ashkenasi, Appl. Phys. A: Mater. Sci. Process. **69**, 373 (1999).
[25]M. Lenzner, J. Krüger, W. Kautek, and F. Krausz, Appl. Phys. A: Mater. Sci. Process. **69**, 465 (1999).
[26]D. Ashkenasi, M. Lorenz, R. Stoian, and a Rosenfeld, Appl. Surf. Sci. **150**, 101 (1999).
[27]M. Lenzner, J. Krüger, W. Kautek, and F. Krausz, Appl. Phys. A **68**, 369 (1999).
[28]J. Bonse, J. M. Wrobel, J. Krüger, and W. Kautek, Appl. Phys. A: Mater. Sci. Process. **72**, 89 (2001).
[29]A. Ben-Yakar and R. L. Byer, J. Appl. Phys. **96**, 5316 (2004).
[30]L. G. Deshazer, B. E. Newnam, and K. M. Leung, Appl. Phys. Lett. **23**, 607 (1973).
[31]S. Martin, A. Hertwig, M. Lenzner, J. Krüger, and W. Kautek, Appl. Phys. A: Mater. Sci. Process. **77**, 883 (2003).
[32]B. Stuart, M. Feit, S. Herman, A. Rubenchik, B. Shore, and M. Perry, Phys. Rev. B - Condens. Matter Mater. Phys. **53**, 1749 (1996).
[33]M. D. Perry, B. C. Stuart, P. S. Banks, M. D. Feit, V. Yanovsky, and A. M. Rubenchik, J. Appl. Phys. **85**, 6803 (1999).